# Theoretical prediction of low-energy Stone-Wales graphene with an intrinsic type-III Dirac cone

Zhenhao Gong,[*] Xizhi Shi,[*] Jin Li,[†] Shifang Li, Chaoyu He,[‡] Tao Ouyang, Chunxiao Zhang, Chao Tang, and Jianxin Zhong

*Hunan Key Laboratory of Micro-Nano Energy Materials and Devices, Xiangtan University, Hunan 411105, People's Republic of China
and Laboratory for Quantum Engineering and Micro-Nano Energy Technology and School of Physics and Optoelectronics,
Xiangtan University, Hunan 411105, People's Republic of China*

Based on first principles, we predict a new low-energy Stone-Wales graphene SW40, which has an orthorhombic lattice with *Pbam* symmetry and 40 carbon atoms in its crystalline cell forming well-arranged Stone-Wales patterns. The calculated total energy of SW40 is just about 133 meV higher than that of graphene, indicating that its excellent stability exceeds all the previously proposed graphene allotropes. We find that SW40 exhibits an intrinsic type-III Dirac cone [Phys. Rev. Lett. **120**, 237403 (2018)] formed by band crossing of local linear and flat bands, which can result in highly anisotropic fermions in the system. Interestingly, such an intrinsic type-III Dirac cone can be effectively tuned by inner-layer strain and it will be transferred into type-I and type-II Dirac cones under tensile and compressed strain, respectively. Finally, a general tight-binding model was constructed to understand the electronic properties near the Fermi level in SW40. The results show that type-III Dirac cone features can be well understood by the $\pi$-electron interactions between adjacent Stone-Wales defects.

## I. INTRODUCTION

The experimental synthesis of two-dimensional (2D) graphene [1–3] and graphdiynes [4,5] opened the door to the 2D carbon word and has attracted much scientific efforts to reveal their fundamental properties and potential applications [1,6–9]. With excellent mechanical and electronic properties [1,6,7], graphene is believed to be a potential candidate for replacing silicon in future nanoelectronics as a new building block [10]. 2D carbon allotropes can provide us with rich electronic properties for different functional requirements needed to design pure-carbon nanodevices. For example, $R_{57-1}$ [11], $R_{57-2}$ [12], $H_{567}$ [12], $O_{567}$ [12], $\psi$-graphene [13,14], OPG-L [15], net-$\tau$ [16], and other 2D carbon allotropes [17–25] with normal metallic properties can be used as electron conductors. The semiconducting octite SC [20], pza-C10 [26], $\Theta$-graphene [27,28], and $\gamma$-graphyne [29,30] are proper candidates [24,31,32] for building diodes and transistors. The graphene [1–3], phagraphene [33], OPG-Z [15], and SW-graphene [24] as Dirac cone semimetals [24,31,32,34] with high carrier mobility can be used to construct high-speed nanodevices. Especially, the freedom of rotation in graphene bilayer bring us a surprising phenomenon of superconductivity at some magic angles [35–38]. This fact has set off a new round of research upsurge on low-dimensional carbon systems [39–42].

Recently, highly anisotropic Dirac cones have attracted tremendous attentions because of their effect on direction-dependent optical and electronic properties [43]. It is reported that the anisotropic band dispersions can be induced in graphene through external periodic potentials [44,45] or elemental doping [46]. In fact, intrinsic anisotropic Dirac cones can be realized through graphene [15,24,33] and graphyne [32,42,47,48] allotropes, such as OPG-Z [15], phagraphene [33], and SW-graphene [24]. However, the anisotropies of the Dirac cones are usually not very strong. Recently, new types of Dirac cones, i.e., type-II [49–52] and type-III Dirac cones [53], have been proposed and attracted tremendous attention. These new types of Dirac fermions have different properties than type-I Dirac fermions [49], in particular, they exhibit highly anisotropic Fermi velocities around the Dirac cone. However, the type-II and type-III Dirac fermions seem to be much less common than the type-I Dirac fermions in pure 2D carbon systems. We notice that only OPG-Z [15] possesses remarkable anisotropic properties due to its type-III-like Dirac cone [53], however, its calculated total energy is 345 meV/atom higher than that of graphene, indicating that it is difficult to synthesize it in future experiments. Therefore, to theoretically propose experimentally viable 2D carbons with type-II or type-III Dirac fermions [53] and highly anisotropic properties is of crucial importance for both fundamental and practical interests.

In this work, we report our discovery of new Stone-Wales graphene (SW40) with an intrinsic type-III Dirac cone and excellent stability. SW40 contains 40 carbon atoms in its orthorhombic crystalline cell and well-arranged Stones-Wales patterns. Its calculated total energy is only 133 meV/atom higher than that of graphene and lower than those of all the previously predicted 2D carbons. The calculated electronic properties reveal that SW40 exhibits the intrinsic type-III Dirac cone formed by band crossing of local linear and local flat bands. Such an intrinsic type-III Dirac cone can be effectively tuned by the in-plane strain and it will be transferred into type-II and type-I Dirac cones under tensile and compressed strain, respectively. Finally, a general

[*]These authors contributed equally to this work.

[†]lijin@xtu.edu.cn

[‡]hechaoyu@xtu.edu.cn

FIG. 1. The optimized crystalline structures of the 30 newly discovered 2D carbons together with their names (sn-in-tn-rs) and energies (eV per atom). The nomenclature of "sn-in-tn-rs" is designed to reveal the fundamental crystal information of the space group number (sn), inequivalent atom number (in), total atom number (tn), and carbon ring sequence (rs). (Top right) The calculated total energies of all the previously predicted (red solid circles) and the newly discovered (blue solid hexagons) 2D carbon allotropes plotted as functions of the corresponding carbon densities.

tight-binding model was constructed to explore the Dirac cone features in SW40, which can be understood by including the interactions between adjacent Stone-Wales defects.

## II. METHODOLOGIES

To search new 2D carbon allotropes with both remarkable stability and highly anisotropic Dirac cone, we performed stochastic group and graph constrained searches [54,55] based on our previously developed RG$^2$ code [24,56,57], which is a highly efficient code for generating crystal structures with well-defined structural features [58–62]. The first-principles calculations are performed by the widely used VASP code [63], with the projector augmented wave methods (PAW) [64,65] and the generalized gradient approximation (GGA) [66]. A plane-wave basis with cutoff energy of 500 eV is used to expand the wave functions for all carbon systems and the Brillouin zone sampling meshes are set to be dense enough to ensure the convergence ($11 \times 11 \times 1$ for SW40). All the 2D carbon structures are fully optimized until the residual forces on every atom is less than 0.001 eV/Å. The convergence

criterion of total energy is set to be $10^{-7}$ eV and the thickness of the slab model is set to be larger than 15 Å to avoid spurious interactions between adjacent images. The open-free PHONOPY code [67] is employed to simulate the vibrational spectrum of SW40.

## III. STRUCTURES AND STABILITIES

Our RG$^2$ searching process generated 90 unequal 2D $sp^2$ carbons including most of all the previously predicted ones and 30 new allotropes as shown in Fig. 1 and Fig. S1 [68]. To reveal their fundamental structural information, all the 2D carbon allotropes are named as "sn-in-tn-rs" according to their space group numbers (sn), inequivalent atom numbers (in), total atom numbers (tn), and ring sequences (rs). With such an uniform nomenclature, it is convenient to manage the structures in future research works of citation and repetition judgment [69]. The topology information of these 2D carbon allotropes can be quickly calculated by the RG$^2$ code [56] or TOPOSPRO SOFT [70,71] and it is summarized in Table S1 in Ref. [68] in a simple organizational form similar to those in
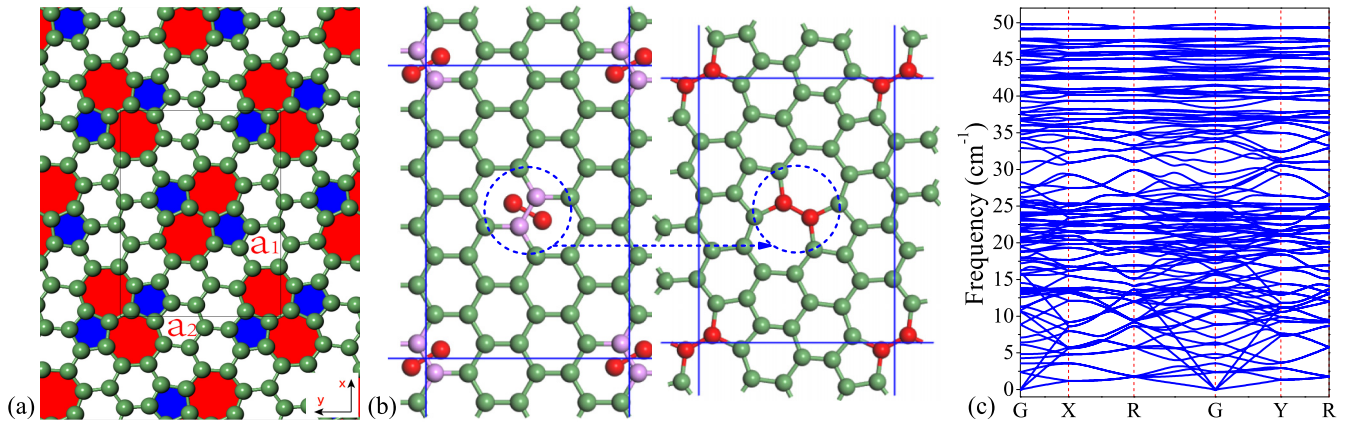
FIG. 2. (a) The optimized crystal structure of SW40 with well-arranged Stone-Wales defects as colored in blue and red. (b) The potential structural transition pathway from a given graphene supercell to SW40. (c) The calculated phonon band structure of SW40.

previous work [72]. The names of the newly discovered 30 2D carbons are shown in Fig. 1 together with their optimized crystal structures and the corresponding total energies relative to graphene. We can see that these newly discovered 2D carbon allotropes are all three-connected and they contain mixed 4-, 5-, 6-, 7-, 8-, and 9-member rings in their bodies. It is noticed that 55-10-40-r567-1 can be considered as a new Stone-Wales graphene [24] with well-arranged Stone-Wales defects in its body as shown in Fig. 2(a) and we further share it a short name of SW40 according to its total atom number. As shown in Fig. 2(b), the new discovered SW40 has another structural feature that can be structurally constructed through a 90° rotation of a carbon dimmer in a given orthorhombic supercell of graphene. Such a structural feature is very similar to the previously predicted SW-graphene [24], Pza-C10 [26], $R_{57-2}$ [12], and OPG-Z [15] as shown in Fig. S2 [68].

To discuss the relative stabilities of these newly discovered 2D carbon allotropes,their calculated total energies relative to graphene are plotted in Fig. 1 together with the corresponding carbon densities. The results show that most of these newly discovered 2D carbons are more stable than the previously proposed T-graphene (518 meV/atom) [21–23]. Especially, the total energy of SW40 is only about 133 meV higher than that of graphene and it is lower than those of all the previously predicted 2D carbon structures, including the recently synthesized phagraphene (201 meV/atom) and TPH-graphene (419 meV/atom) [74]. Such an excellent stability indicates that SW40 is an expectable target for future experiments.

The vibrational spectrum of SW40 was calculated to evaluate its dynamical stability as shown in Fig. 2(c). There are no negative frequencies appearing in the phonon band structure, indicating that SW40 is dynamically stable under small vibrations. The thermal stability of SW40 is also investigated by *ab initio* molecular dynamics simulations using a $2 \times 3 \times 1$ supercell. After heating at 300 and 500 K for 5 ps with a time step of 1 fs, the structure of SW40 remains intact and the total energies only oscillate about a constant value as shown in Fig. S3 [68]. Such results suggest that SW40 crystal is thermally stable at room temperature. Since 2D graphene with Stone-Wales defects has been synthesized in experiments [73] and the periodic nonhexagonal carbon rings have been realized in graphene nanoribbons [74,75],

SW40 is expected to be realized in the future. It is noticed that the previously proposed phagraphene [33] and TPH-graphene [74] were recently synthesized [74] by the widely used molecular assembly [76,77] method. Thus it is highly possible that SW40 can be realized through an assembly of ethylene and benzene (or naphthalene and azulene) as shown in Fig. S4 [68].

## IV. ELECTRONIC PROPERTIES

Figure 3(a) shows the DFT-based band structure of SW40 in the first BZ along high-symmetry $k$ path $\Gamma(0, 0) \rightarrow X(0.5, 0) \rightarrow R(0.5, 0.5) \rightarrow Y(0, 0.5)$. It is interesting that
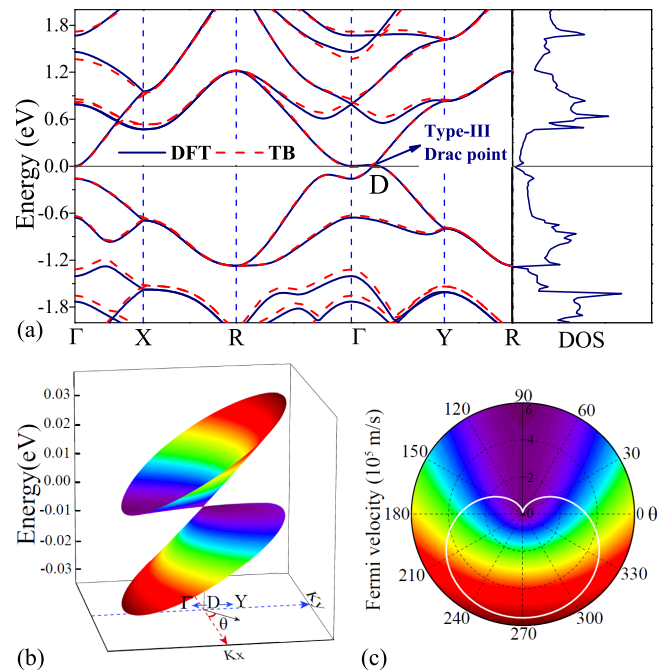


FIG. 3. (a) Electronic band structures and density of states of SW40 from DFT (blue) and TB (red) calculations. (b) The 3D band structures of SW40 near the Dirac point to show its Dirac cone features. (c) The direction-dependent Fermi velocities calculated based on DFT results (white line).

there is a distorted Dirac point [locating at D (0, 0.115)] formed by the crossing of the local linear and local flat bands at the Fermi level. To further confirm such a band crossing, the decomposed charge densities near the Dirac point are calculated and shown in Fig. S5 [68]. One can see that the charge densities at the two sides of the Dirac point are inverted, suggesting that the Dirac point in SW40 is formed by band crossing. Furthermore, the calculated density of state (DOS) at the Fermi level with the value of zero can also confirm that SW40 is a semimetal with the Dirac point formed by band crossing.

The DFT-based 3D surface band structure of SW40 near the Dirac point is plotted in Fig. 3(b) and it clearly shows that there is a distorted Dirac cone. We can see that the distorted Dirac cone in SW40 is formed by the crossing of the local linear and a local flat bands, which is somewhat different from the type-I cones in graphene, phagraphene, and SW-graphene. As discussed by Liu *et al.* in their recent work [53], such a distorted Dirac cone with a local flat band can be classified as a type-III Dirac cone, and it can be realized in compressively strained BP under a periodic field of a circularly polarized laser, thus providing us with a new type of Fermion quasiparticles. We notice that such a new type of Dirac cone (type III) in the SW40 is intrinsic and it had been reported in previously proposed OPG-Z [15]. Given its excellent stability exceeding that of OPG-Z (348 meV/atom), SW40 (133 meV/atom) with the intrinsic type-III Dirac cone is expected to be a highly anticipated experimental target for realizing new fermion quasiparticles.

Another significant feature of the type-III Dirac cone is the high anisotropy. As shown in the 3D surface band structure, both the occupied and unoccupied bands near the Dirac point show very different slopes in different directions. To evaluate the anisotropy of the type-III Dirac cone in SW40, we calculate the direction-dependent Fermi velocities in the cone as $v_f = E(k)/\hbar|k|$. As shown in Fig. 3(c), the Fermi velocity of the new fermions in SW40 nearby the Dirac cone is strongly anisotropic with a heartlike shape. They are characterized by strongly varying Fermi velocities from $2.611 \times 10^3$ m/s along the $-y(\theta = 90°)$ direction to $5.697 \times 10^5$ m/s along to the $+y(\theta = 270°)$ direction. The anisotropy of the Dirac cone [A(D)] can be defined as A(D) = $(v_{max}(\theta) - v_{min}(\theta))/(v_{max}(\theta) + v_{min}(\theta))$, where $v_{max}(\theta)$ and $v_{min}(\theta)$ are the maximum and minimum direction-dependent Fermi velocities in the cone [78]. Based on the data in Fig. 3(c), we can easily obtain the anisotropy of the type-III Dirac cone in SW40 of A(D) = 99.09%, which is gigantic in comparison with those in graphene- and graphyne-type materials [78]. The intrinsic type-III Dirac cone with strong anisotropy, free from extra manipulating efforts, will broaden potential applications of SW40 in information applications.

It is interesting that the properties of the type-III Dirac cone in SW40 can be effectively tuned by external strain. Figure 4(a) shows partial band structures of SW40 along $\Gamma$-$Y$ $k$ path under selected biaxial in-plane strain (−8%, −3%, −1%, 0%, 1%, 3%, and 8%). We can see that the Dirac cone in SW40 can survive in different strain but the curvatures of the two energy bands near the crossing point are significantly changed, resulting in two transitions from type III to type I in tensile strain and type III to type II in compressive strain,
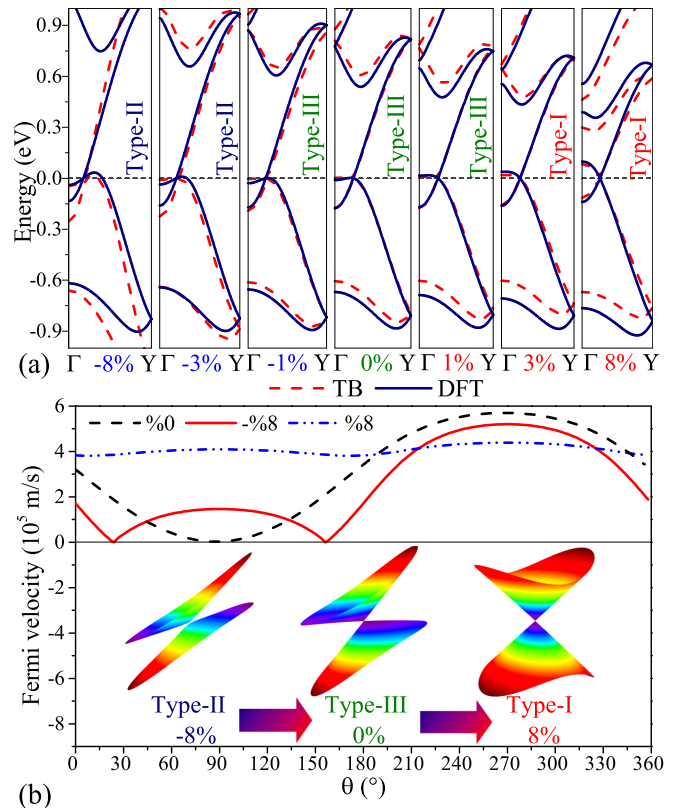


FIG. 4. (a) The DFT-based (blue solid lines) and TB-based (red dash lines) band structures of SW40 under selected strain (−8%, −3%, −1%, 0%, 1%, 3%, and 8%). (b) The direction-dependent Fermi velocities in type-II (−8%), type-III (0%), and type-I (8%) Dirac cones and the corresponding 3D plots of the cones.

respectively. Under tensile strain, it is found that the curvatures of the two bands near the crossing point are just slightly modulated. However, these two crossing bands move closer to each other (from $Y$ point) and correspondingly shift the crossing point far away from the local flat band to gradually form a type-I Dirac cone under tensile strain.

The shapes of the two crossing bands are obviously changed and they move apart from each other (from the $Y$ point) under compressive stain, which destroy the type-III Dirac cone features and form a new type-II Dirac point in $\Gamma$-$Y$. As shown in Fig. 4(b), we have also calculated 3D band structures to confirm the Dirac cone features in SW40 under strain −8%, 0%, and 8%, respectively. The corresponding direction-dependent Fermi velocities in Fig. 4(b) show that tensile strain will weaken the anisotropy of the Dirac cone and the compressive strain will enhance it. In Fig. S6 [68], the results suggest that the type-III Dirac cone feature in SW40 can survive in the strain range from −1% to 2%, the transition points from type III to type II and type I are with compressive −2% and tensile 3% strain, respectively.

## V. TIGHT-BINDING MODEL

To further understand the DFT-based results, we adopted a general tight-binding (TB) model based on the Slater-Koster method to describe the electrons in SW40 near the Fermi level. As the electronic states around the Fermi level are

TABLE I. The optimal values of $V_{pp\pi}$, $S_{pp\pi}$, $q_1$, and $q_2$ determined under different cutoff distances ($d_{cut}$) and the corresponding standard deviations $\chi(vc)$. The corresponding band structures are shown in Fig. S8 and their corresponding Dirac cone type (DT) are marked in this table.

| $d_{cut}$ | $V_{pp\pi}$ | $S_{pp\pi}$ | $q_1$ | $q_2$ | $\chi(vc)$ | BS | DT |
|---|---|---|---|---|---|---|---|
| 2 | −2.354 | 0.0356 | 5.003 | 1.216 | 0.08803 | Fig. S8(a) | Type I |
| 4 | −1.909 | 0.4628 | 1.794 | 2.136 | 0.03854 | Fig. S8(b) | Type I |
| 6 | −2.431 | 0.3151 | 1.427 | 1.349 | 0.02702 | Fig. S8(c) | Type I |
| 8 | −1.819 | 0.4621 | 1.358 | 1.205 | 0.01837 | Fig. S8(d) | Type III |
| 10 | −1.786 | 0.4767 | 1.274 | 1.183 | 0.01855 | Fig. S8(e) | Type III |
| 12 | −1.753 | 0.4913 | 1.192 | 1.161 | 0.01724 | Fig. S8(f) | Type III |

predominantly contributed by $p_z$ orbitals of C atom, only C-$p_z$ orbitals are included in the TB model. The TB Hamiltonian could be generally written as

$$H = -\sum_{i\neq j} t_{ij}(c_i^\dagger c_j + \text{H.c.}) + \varepsilon_\pi \sum_i c_i^\dagger c_i,$$
$$= \sum_{i\neq j} s_{ij}(c_i^\dagger c_j + \text{H.c.}) + \sum_i c_i^\dagger c_i \qquad (1)$$

where $t_{ij}$ and $s_{ij}$ are respectively the hopping and overlap integrals of an electron between the $i$th and $j$th atoms and $c_i^\dagger$ and $c_j$ are the creation and annihilation operators, respectively. Because all atoms are carbon, the on-site energy $\varepsilon_\pi$ can be set to 0 eV. The distance-dependent hopping and overlap integrals are determined by the formula

$$t_{ij} = V_{pp\pi} e^{q_1 \times (1-d_{ij}/d_0)} \text{ and } s_{ij} = S_{pp\pi} e^{q_2 \times (1-d_{ij}/d_0)}. \qquad (2)$$

Here, $d_0$ is the reference distance and set to be the length of standard C-C bond (1.426 Å) in graphene, $V_{pp\pi}$ and $S_{pp\pi}$ are respectively the hopping and overlap integrals between $p$ orbitals at $d_0$. $d_{ij}$ is the distance between the $i$th and $j$th atoms and $q_{1,2}$ are the decay constants for the integrals. As $d_{ij}$ is larger than the used cutoff distance $d_{cut}$, these integrals are set to be 0. These tight-binding parameters are fitted by minimizing the standard deviation function $\chi(V_{pp\pi}, S_{pp\pi}, q_1, q_2)$ as

$$\chi(\sigma) = \sqrt{\frac{1}{N_{data}} \sum_{n,k} \left[ \mu_{n,k} \times \left( E_{n,k}^{TB} - E_{n,k}^{DFT} \right) \right]^2}, \qquad (3)$$

where $E_{n,k}^{TB}$ and $E_{n,k}^{DFT}$ are the $n$th TB-based and DFT-based eigenvalues relative to the corresponding Fermi level at the used $k$ point. $\mu_{n,k}=1$ ($|E_{n,k}^{DFT}| < \sigma$) or 0 ($|E_{n,k}^{DFT}| > \sigma$), depending on the used cutoff energy $\sigma$. $N_{data}$ is the total number of data points in the energy area from $-\sigma$ eV to $\sigma$ eV for all the used $k$ points.

We have fit the above parameters with the cutoff distance ($d_{cut}$) range from 2, 4, 8, 10, and 12 Å (as indicated in Fig. S7 [68]) by minimizing the deviation function $\chi(vc)$ ($\sigma \approx 1.2$) of the first valence and the first conduction bands. The finally optimal parameters under $d_{cut}$ are summarized in Table I together with their $\chi(vc)$ and the corresponding band structures are shown in Figs. S8(a)–S8(h) compared with the DFT-based results [68]. We can see that under $d_{cut}$ of 2 Å, the optimized parameters can not describe the band structures of SW40 well [$\chi(vc) = 88$ meV, high anisotropy,

type I]. The optimized parameters under $d_{cut}$ of 4 and 6 Å can approximatively describe the band structures nearby the Fermi level with the standard deviations $\chi(vc)$ of about 38 and 27 meV, respectively. However, they both are type I with high anisotropy and can not fit the DFT-based type-III Dirac point. Parameters obtained under $d_{cut}$ of 8, 10, and 12 Å can fit the DFT results well, resulting in the type-III Dirac point and low standard deviation $\chi(\sigma)$ of about 18 meV. Such an excellent agrement can be understood according to the fact that these $d_{cut}$ are greater than 7.445 Å, which are large enough to include the interactions between adjacent Stone-Wales defects.

The $\sigma$-dependent standard deviations $\chi(\sigma)$ shown in Fig. S7 suggest that the parameters optimized under $d_{cut}$s of 8, 10, and 12 Å can fit the DFT-based band structures very well in the energy range from $-1.5$ to $1.5$ eV. In larger energy range from $-3.75$ to $3.75$ eV, these parameters can also repeat the DFT-based band structure well with slightly enlarged standard deviations $\chi(\sigma)$. As shown in Fig. S9 [68], the parameters obtained from $d_{cut}$ smaller than 7.445 Å can not fit the DFT-based bands when we use larger $d_{cut}$ for calculation. The parameters can be improved at $d_{cut}$ of 8 Å and the standard deviation $\chi(vb)$ can achieve good convergence in 10 and 12 Å. For $sp^2$ hybridized carbon systems, we care about only the energy area nearby the Fermi level, especially the first valance and the first conduction bands. Thus we finally suggest using the parameters optimized under $d_{cut}$ of 10 Å to investigate the band structure of SW40. Based on such optimal parameters under $d_{cut}$ of 10 Å, we calculated the band structures of SW40 using different $d_{cut}$ of 8, 6, 5, 4, 3, and 2 Å as shown in Fig. S10 [68] together with the corresponding standard deviations. We can see that it is difficult to describe the band structure of SW40, especially the type-III Dirac cone feature, if we do not include the interactions between adjacent Stone-Wales defects (7.445 Å).

We have also estimated the transferability of the final used parameters obtained from $d_{cut} = 10$ Å by comparing the DFT-based and TB-based band structures of some previously predicted 2D carbons as shown in Fig. S11 [68]. The used test structures include metals (Octite-M1 [19] and H$_{567}$ [12]), semimetals (phagraphene [33] and SW-graphene [24]), and semiconductors (Octite SC [20], and Θ-graphene [27,28]) with different symmetries (hexagonal, tetragonal, and orthorhombic). We can see that the parameters can commendably fit the DFT-based band structures nearby the Fermi level, leaving relatively small standard deviations ($\chi$). However, we find that these parameters can not directly repeat the strain effects on the band structure of SW40 well. Thus we further introduce two quadratic polynomials [79] to include additional strain-induced decaying functions for $V_{pp\pi}$ and $S_{pp\pi}$ as discussed in Ref. [68]. As shown in Fig. 4(a) and Fig. S6 in Ref. [68], the modulating effects of external strain on the band structures SW40, including the transition of type III to type I and type III to type II, can be well described.

## VI. CONCLUSION

In conclusion, we propose a new 2D carbon candidate SW40 by employing our previously developed RG$^2$ code and the widely used VASP code. SW40 contains 40 carbon atoms

in its orthorhombic lattice with *Pbam* symmetry, forming well-arranged Stone-Wales patterns. Our results show that the total energy of SW40 is about 133 meV/atom above that of graphene, indicating that it is more stable than all the previously predicted 2D carbons. The detailed analysis of electronic properties reveals that SW40 processes intrinsic type-III Dirac cone with high anisotropy. Such a type-III Dirac cone can by effectively modulated, with two transitions from type III to type I in tensile strain and type III to type II in compressive strain, respectively. Finally, a general tight-binding model based on the Slater-Koster method was constructed and our TB results reveal that a highly anisotropic type-III Dirac cone in SW40 can be well understood by the interaction between adjacent Stone-Wales defects.

[1] K. S. Novoselov, A. K. Geim, S. V. Morozov, D. Jiang, Y. Zhang, S. V. Dubonos, I. V. Grigorieva, and A. A. Firsov, Science **306**, 666 (2004).

[2] K. S. Kim, Y. Zhao, H. Jang, S. Y. Lee, J. M. Kim, K. S. Kim, J. H. Ahn, P. Kim, J. Y. Choi, and B. H. Hong, Nature (London) **457**, 706 (2009).

[3] Z. Z. Sun, Z. Yan, J. Yao, E. Beitler, Y. Zhu, and J. M. Tour, Nature (London) **468**, 549 (2010).

[4] G. Li, Y. Li, H. Liu, Y. Guo, Y. Li, and D. Zhu, Chem. Commun. **46**, 3256 (2010).

[5] R. Matsuoka, R. Sakamoto, K. Hoshiko, S. Sasaki, H. Masunaga, K. Nagashio, and H. Nishihara, J. Am. Chem. Soc. **139**, 3145 (2017).

[6] Y. Zhang, Y.-W. Tan, H. L. Stormer, and P. Kim, Nature (London) **438**, 201 (2005).

[7] K. I. Bolotin, F. Ghahari, M. D. Shulman, H. L. Stormer, and P. Kim, Nature (London) **462**, 196 (2009).

[8] K. S. Novoselov, Z. Jiang, Y. Zhang, S. V. Morozov, H. L. Stormer, U. Zeitler, J. C. Maan, G. S. Boebinger, P. Kim, and A. K. Geim, Science **315**, 1379 (2007).

[9] K. S. Novoselov, E. McCann, S. V. Morozov, V. I. Fal'ko, M. I. Katsnelson, U. Zeitler, D. Jiang, F. Schedin, and A. K. Geim, Nat. Phys. **2**, 177 (2006).

[10] R. V. Noorden, Moving towards a graphene world, Nature (London) **442**, 228 (2006).

[11] V. H. Crespi, L. X. Benedict, M. L. Cohen, and S. G. Louie, Phys. Rev. B **53**, R13303 (1996).

[12] H. Terrones, M. Terrones, E. Hernández, N. Grobert, J-C. Charlier, and P. M. Ajayan, Phys. Rev. Lett. **84**, 1716 (2000).

[13] G. Csányi, C. J. Pickard, B. D. Simons, and R. J. Needs, Phys. Rev. B **75**, 085432 (2007).

[14] X. Y. Li, Q. Wang, and P. Jena, J. Phys. Chem. Lett. **8**, 3234 (2017).

[15] C. Su, h. Jiang, and J. Feng, Phys. Rev. B **87**, 075453 (2013).

[16] X. Wang, Z. H. Feng, J. Rong, Y. N. Zhang, Y. Zhong, J. Feng, X. H. Yu, and Z. L. Zhan, Carbon **142**, 438 (2019).

[17] M. T. Lusk and L. D. Carr, Phys. Rev. Lett. **100**, 175503 (2008).

[18] M. T. Lusk, and L. D. Carr, Carbon **47**, 2226 (2009).

[19] D. J. Appelhans, L. D. Carr, and M. T. Lusk, New. J. Phys. **12**, 125006 (2010).

[20] D. J. Appelhans, Z. B. Lin, and M. T. Lusk, Phys. Rev. B **82**, 073410 (2010).

[21] J. Nisar, X. Jiang, B. Pathak, J. J. Zhao, T. W. Kang, and R. Ahuja, Nanotechnology **23**, 385704 (2012).

[22] X. Q. Wang, H. D. Li, and J. T. Wang, Phys. Chem. Chem. Phys. **14**, 11107 (2012).

[23] Y. Liu, G. Wang, Q. S. Huang, L. W. Guo, and X. L. Chen, Phys. Rev. Lett. **108**, 225505 (2012).

[24] H. C. Yin, X. Shi, C. He, M. Martinez-Canales, J. Li, C. J. Pickard, C. Tang, T. Ouyang, C. Zhang, and J. Zhong, Phys. Rev. B **99**, 041405(R) (2019).

[25] C. X. Zhao, Y. Q. Yang, C. Y. Niu, J. Q. Wang, and Y. Jia, Comput. Mater. Sci. **160**, 115 (2019).

[26] X. G. Luo, L. M. Liu, Z. P. hu, W. H. Wang, W. X. Song, F. F. Li, S. J. Zhao, H. Liu, H. T. Wang, and Y. J. Tian, J. Phys. Chem. Lett. **3**, 3373 (2012).

[27] W. C. Yi, W. Liu, J. Botana, J. Y. Liu, and M. S. Miao, J. Mater. Chem. A **6**, 10348 (2018).

[28] S. W. Wang, B. C. Yang, H. Y. Chen, and E. Ruckenstein, Energy Storage Mater. **16**, 619 (2019).

[29] B. G. Kim and H. J. Choi, Phys. Rev. B **86**, 115435 (2012).

[30] H. Q. Huang, W. H. Duan, and Z. R. Liu, New J. Phys. **15**, 023004 (2013).

[31] W. Liu, L. Zhao, E. Zurek, J. Xia, Y. H. Zheng, H. Q. Lin, J. Y. Liu, and M. S. Miao, npj Comput. Mater. **5**, 71 (2019).

[32] M. Park, Y. Kim, and H. Lee, npj Comput. Mater. **4**, 54 (2018).

[33] Z. H. Wang, X. F. Zhou, X. M. Zhang, Q. Zhu, H. F. Dong, M. W. Zhao, and A. R. Oganov, Nano Lett. **15**, 6182 (2015).

[34] J. Liu and H. G. Lu, RSC Adv. **9**, 34481 (2019).

[35] Y. Cao, V. Fatemi, S. Fang, K. Watanabe, T. Taniguchi, E. Kaxiras, and P. Jarillo-Herrero, Nature (London) **556**, 43 (2018).

[36] Y. Cao, V. Fatemi, A. Demir, S. Fang, S. L. Tomarken, J. Y. Luo, J. D. Sanchez-Yamagishi, K. Watanabe, T. Taniguchi, E. Kaxiras, R. C. Ashoori, and P. Jarillo-Herrero, Nature (London) **556**, 80 (2018).

[37] A. Kerelsky, L. J. McGilly, D. M. Kennes, L. Xian, M. Yankowitz, S. W. Chen, K. Watanabe, T. Taniguchi, J. Hone, C. Dean, A. Rubio, and A. N. Pasupathy, Nature (London) **572**, 95 (2019).

[38] M. Yankowitz, S. W. Chen, H. Polshyn, Y. X. Zhang, K. Watanabe, T. Taniguchi, D. Graf, A. F. Young, and C. R. Dean, Science **363**, 1059 (2019)

[39] H. C. Po, L. Zou, A. Vishwanath, and T. Senthil, Phys. Rev. X **8**, 031089 (2018).

[40] C. C. Liu, L. D. Zhang, W. Q. Chen, and F. Yang, Phys. Rev. Lett. **121**, 217001 (2018).

[41] F. C. Wu, A. H. MacDonald, and I. Martin, Phys. Rev. Lett. **121**, 257001 (2018).

[42] Y. P. Chen, S. L. Xu, Y. Xie, C. Y. Zhong, C. J. Wu, and S. B. Zhang, Phys. Rev. B **98**, 035135 (2018).

[43] F. N. Xia, H. Wang, and Y. C. Jia, Nat. Commun. **5**, 4458 (2014).

[44] C. H. Park, L. Yang, Y. W. Son, M. L. Cohen, and S. G. Louie, Nat. Phys. **4**, 213 (2008)

[45] C. H. Park, L. Yang, Y. W. Son, M. L. Cohen, and S. G. Louie, Phys. Rev. Lett. **101**, 126804 (2008).

[46] H. H. Zhang, Y. Xie, C. Y. Zhong, Z. W. Zhang, and Y. P. Chen, J. Phys. Chem. C **121**, 12476 (2017).

[47] N. V. R. Nulakani and V. Subramanian, ACS Omega **2**, 6822 (2017).

[48] L. Z. Zhang, Z. F. Wang, Zhiming M. Wang, S. X. Du, H.-J. Gao, and F. Liu, J. Phys. Chem. Lett. **6**, 2959 (2015).

[49] H. Q. Huang, S. Y. Zhou, and W. H. Duan, Phys. Rev. B **94**, 121117(R) (2016).

[50] L. Muechler, A. Alexandradinata, T. Neupert, and R. Car, Phys. Rev. X **6**, 041069 (2016).

[51] A. S. Cuamba, P. Hosur, H. Y. Lu, L. Hao, and C. S. Ting, Phys. Rev. B **96**, 195159 (2017).

[52] K. Deng, G. L. Wan, P. Deng, K. N. Zhang, S. J. Ding, E. Y. Wang, M. Z. Yan, H. Q. Huang, H. Y. Zhang, Z. L. Xu, J. Denlinger, A. Fedorov, H. T. Yang, W. H. Duan, H. Yao, Y. Wu, S. S. Fan, H. J. Zhang, X. Chen, and S. Y. Zhou, Nat. Phys. **12**, 1105 (2016).

[53] H. Liu, J. T. Sun, C. Cheng, F. Liu, and S. Meng, Phys. Rev. Lett. **120**, 237403 (2018).

[54] C. J. Pickard, and R. J. Needs, J. Phys.: Condens. Matter **23**, 053201 (2011).

[55] R. T. Strong, C. J. Pickard, V. Milman, G. Thimm, and B. Winkler, Phys. Rev. B **70**, 045101 (2004).

[56] X. Z. Shi, C. Y. He, C. J. Pickard, C. Tang, and J. X. Zhong, Phys. Rev. B **97**, 014104 (2018).

[57] C. Y. He, X. Z. Shi, S. J. Clark, J. Li, C. J. Pickard, T. Ouyang, C. X. Zhang, C. Tang, and J. X. Zhong, Phys. Rev. Lett. **121**, 175701 (2018).

[58] P. L. Sun, C. Y. He, C. X. Zhang, H. P. Xiao, and J. X. Zhong, Phys. B: Condens. Matter **562**, 131 (2019).

[59] N. Jiao, P. Zhou, C. Y. He, J. J. He, X. L. Liu, and L. Z. Sun, Phys. Status. Solidi-RRL **13**, 1900470 (2019).

[60] Z. Q. Li, X. Z. Shi, C. Y. He, T. Ouyang, J. Li, C. X. Zhang, S. F. Zhang, C. Tang, R. A. Römer, and J. X. Zhong, Appl. Surf. Sci. **497**, 143803 (2019).

[61] N. Zhou, P. Zhou, J. Li, C. Y. He, and J. X. Zhong, Phys. Rev. B **100**, 115425 (2019).

[62] X. Yang, C. Y. He, X. Z. Shi, J. Li, C. X. Zhang, C. Tang, and J. X. Zhong, J. Appl. Phys. **124**, 163107 (2018).

[63] G. Kresse and J. Furthmüller, Phys. Rev. B **54**, 11169 (1996).

[64] P. E. Blöchl, Phys. Rev. B **50**, 17953 (1994).

[65] G. Kresse and D. Joubert, Phys. Rev. B **59**, 1758 (1999).

[66] J. P. Perdew, K. Burke, and M. Ernzerhof, Phys. Rev. Lett. **77**, 3865 (1996).

[67] Phonopy: http://atztogo.github.io/phonopy/.

[68] See Supplemental Material at http://link.aps.org/supplemental/10.1103/PhysRevB.101.155427 for additional discussions about structures, stabilities, electronic properties, as well as the tight-binding method.

[69] R. Hoffmann, A. A. Kabanov, A. A. Golov, and D. M. Proserpio, Angew. Chem., Int. Ed. **55**, 10962 (2016).

[70] V. A. Blatov, A. P. Shevchenko, and D. M. Proserpio, Cryst. Growth Des. **14**, 3576 (2014).

[71] http://topospro.com/software/.

[72] V. L. Deringer, G. Csányi, and D. M. Proserpio, Chem. Phys. Chem. **18**, 873 (2017).

[73] J. Kotakoski, A. V. Krasheninnikov, U. Kaiser, and J. C. Meyer, Phys. Rev. Lett. **106**, 105505 (2011).

[74] Q. T. Fan, D. Martin-Jimenez, D. Ebeling, C. K. Krug, L. Brechmann, C. Kohlmeyer, G. Hilt, W. Hieringer, A. Schirmeisen, and J. M. Gottfried, J. Am. Chem. Soc. **141**, 17713 (2019).

[75] M. Z. Liu, M. X. Liu, L. M. She, Z. Q. Zha, J. L. Pan, S. C. Li, T. Li, Y. Y. He, Z. Y. Cai, J. B. Wang, Y. Zheng, X. H. Qiu, and D. Y. Zhong, Nat. Commun. **8**, 14924 (2017).

[76] J. V. Barth, G. Costantini, and K. Kern, Nature (London) **437**, 671 (2005).

[77] L. Grill, M. Dyer, L. Lafferentz, M. Persson, M. V. Peters, and S. Hecht, Nat. Nanotechnol. **2**, 687 (2007).

[78] D. Z. Yang, M. S. Si, G. P. Zhang, and D. S. Xue, Europhys. Lett. **107**, 20003 (2014).

[79] G. Gui, J. Li, and J. X. Zhong, Phys. Rev. B **78**, 075435 (2008).